

# Magnetic Anisotropy and Magnetic Ordering of Transition-Metal Phosphorus Trisulfides

Tae Yun Kim\* and Cheol-Hwan Park\*



Cite This: *Nano Lett.* 2021, 21, 10114–10121



Read Online

ACCESS |



Metrics & More



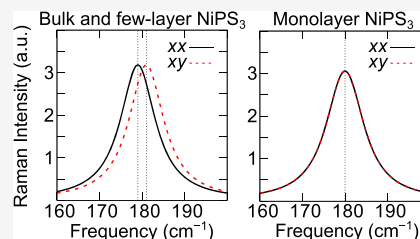
Article Recommendations



Supporting Information

**ABSTRACT:** A magnetic model with an unprecedentedly large number of parameters was determined from first-principles calculations for transition-metal phosphorus trisulfides (TMPS<sub>3</sub>'s), reproducing the measured magnetic ground states of bulk TMPS<sub>3</sub>'s. Our Monte Carlo simulations for the critical temperature, magnetic susceptibility, and specific heat of bulk and few-layer TMPS<sub>3</sub>'s agree well with available experimental data and show that the antiferromagnetic order of TMPS<sub>3</sub>'s persists down to monolayers. Remarkably, the orbital polarization, neglected in recent first-principles studies, dramatically enhances the magnetic anisotropy of FePS<sub>3</sub> by almost 2 orders of magnitude. A recent Raman study [Kim, K., et al. *Nat. Commun.* 2019, 10, 345] claimed that magnetic ordering is absent in monolayer NiPS<sub>3</sub> but simultaneously reported a strong two-magnon continuum; we show that the criterion used to judge magnetic ordering therein is invalid for monolayer NiPS<sub>3</sub>, providing an understanding of the two seemingly contradictory experimental results. The rich predictions on the magnetic susceptibility and specific heat of few-layer TMPS<sub>3</sub>'s await experimental verifications.

**KEYWORDS:** Antiferromagnetism, Two-dimensional magnetic material, Magnetic anisotropy, Transition metal phosphorus trisulfide, Density functional theory + U, Monte Carlo simulation



Since the discovery of ferromagnetic materials Cr<sub>2</sub>Ge<sub>2</sub>Te<sub>6</sub><sup>1</sup> and CrI<sub>3</sub>,<sup>2</sup> there have been a plethora of studies on two-dimensional (2D) ferromagnetic materials. Recently, the research focus of 2D magnetic materials are moving from ferromagnetic 2D materials toward antiferromagnetic 2D materials. As Cr<sub>2</sub>Ge<sub>2</sub>Te<sub>6</sub> and CrI<sub>3</sub> have played the role of first and representative 2D ferromagnetic materials, few-layer transition-metal phosphorus trisulfides (TMPS<sub>3</sub>s) were synthesized first<sup>3–5</sup> and are playing a similar role for 2D antiferromagnetic materials. A series of Raman studies on the stability of magnetic orders in atomically thin TMPS<sub>3</sub> compounds were published recently,<sup>6–9</sup> which have so far been very highly cited reflecting that these first, representative 2D antiferromagnetic materials are of great interest. More recently, the strong coupling between the magnetic order and lights in FePS<sub>3</sub> and NiPS<sub>3</sub> is drawing huge attention.<sup>10–12</sup>

Unlike the case of 2D ferromagnetic materials, whose magnetic properties and anisotropies are relatively well-known, there have been no satisfactory studies on these subjects for 2D antiferromagnetic materials so far. So, it is very timely and of broad importance to understand the magnetic properties, especially magnetic anisotropies, of the first and representative 2D antiferromagnetic materials from theory and first-principles calculations.

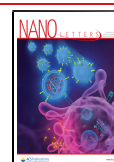
Moreover, there is more interesting physics in these compounds than 2D ferromagnetic materials from the viewpoint of the “magnetism in 2D materials”. According to the Mermin–Wagner theorem,<sup>13</sup> the magnetic ordering in 2D materials depends critically on the kind of detailed interactions among the

magnetic ions: the magnetic ordering at a finite temperature is absent, but there is the so-called Berezinskii–Kosterlitz–Thouless transition<sup>14,15</sup> in 2D XXZ systems. As to investigating this peculiar character of the 2D XXZ model, few-layer NiPS<sub>3</sub>'s were considered an ideal testbed because their antiferromagnetic ordering is believed to be described by the XXZ model.<sup>16</sup> In a recent Raman study,<sup>7</sup> magnetic ordering at a finite temperature of monolayer NiPS<sub>3</sub> was reported to be absent; this conclusion, which was based on their observation of complete absence of the frequency shift of certain peaks in the Raman spectra of monolayer NiPS<sub>3</sub>, seemed to agree with the aforementioned belief: “NiPS<sub>3</sub> is (or at least is very close to) an ideal XXZ system so its magnetic ordering is critically affected by its thickness.” In this perspective, however, it still remained a puzzle that prominent two-magnon signals were also observed in the same Raman spectra of monolayer NiPS<sub>3</sub> at finite temperatures. If the emergence of strong two-magnon continuum in monolayer NiPS<sub>3</sub> is a clear evidence of magnetic ordering at a finite temperature, then why were the frequency shifts of certain Raman peaks, which accompany a magnetic phase transition in the case of bulk NiPS<sub>3</sub>, not detected in the

**Received:** October 15, 2021

**Revised:** November 17, 2021

**Published:** November 24, 2021



ACS Publications

© 2021 American Chemical Society

10114

<https://doi.org/10.1021/acs.nanolett.1c03992>  
Nano Lett. 2021, 21, 10114–10121

case of monolayer NiPS<sub>3</sub> at all although they were all detected in the cases of bilayer or thicker samples as reported in ref 7? Considering that ref 7 has significantly affected the following studies from the viewpoint of applying the Mermin–Wagner theorem to real 2D materials, understanding these seemingly contradictory experimental results is clearly of fundamental importance.

In this paper, we demonstrate that a magnetic model that accurately describes the basic magnetic properties of all three TMPS<sub>3</sub>'s (MnPS<sub>3</sub>, FePS<sub>3</sub>, and NiPS<sub>3</sub>)—ordering pattern, magnetic anisotropy, critical temperature ( $T_N$ ), magnetic susceptibility, and specific heat—can be constructed from density functional theory +  $U$  (DFT+ $U$ ) calculations using fully relativistic pseudopotentials. The magnetic model presented here includes several factors such as the magnetic dipolar anisotropy, orbital degrees of freedom, and interlayer exchange interactions as well as anisotropies in (both intralayer and interlayer) exchange interactions and single-ion anisotropy. On the basis of Monte Carlo simulations, we show that those factors sometimes individually and sometimes as a whole play a crucial role in explaining the magnetic properties of TMPS<sub>3</sub>'s and their thickness dependence.

In the case of TMPS<sub>3</sub>, the magnetic models with up to 10 parameters were considered,<sup>17,18</sup> but still there is no comprehensive magnetic model for TMPS<sub>3</sub> that deals with various kinds of magnetic anisotropies and interlayer exchange interactions simultaneously. Even in a very recent examination of the magnetic anisotropy of CrI<sub>3</sub> (arguably the most famous 2D ferromagnetic material that has been thoroughly studied over the past few years) less than 10 (symmetrically non-equivalent) parameters were considered.<sup>19</sup> Not to mention that a careful consideration of the tensorial form of all the magnetic interactions restricted by the symmetry ( $C2/m$ ) of TMPS<sub>3</sub> was taken here, just the number, 73 parameters for each TMPS<sub>3</sub>, is unprecedentedly large compared to the usual practice of studying magnetic interactions. Here, we demonstrate that our comprehensive magnetic models for TMPS<sub>3</sub>, which took an unprecedented amount of work with respect to the standard of this field, were indeed necessary for us to reach an agreement with available experimental results and several new predictions that would attract the attention of the experimentalists.

Remarkably, we show that the orbital polarization, which was neglected in recent first-principles studies,<sup>18,20</sup> enhances the magnetic anisotropy of FePS<sub>3</sub> by almost 2 orders of magnitude and hence is of crucial importance in explaining the experimental results on its magnetic properties. Moreover, our calculation results predicted magnetic ordering at a finite temperature for monolayer NiPS<sub>3</sub>, whose magnetic ordering was reported to be absent in a recent Raman study.<sup>7</sup> Importantly, we show that the criterion used in the Raman study to detect magnetic ordering does not work in the case of monolayer NiPS<sub>3</sub> and prove the conclusion of the Raman study that there is no magnetic ordering in monolayer NiPS<sub>3</sub><sup>7</sup> to be wrong.

TMPS<sub>3</sub>'s are layered materials (Figure 1a,b) with antiferromagnetic orders that vary with their transition metal (TM = Mn, Fe, and Ni) element.<sup>21</sup> The first constituent of our magnetic model for TMPS<sub>3</sub>'s is the intralayer and interlayer exchange interactions which are written as

$$H_{\text{exch}}^{\text{intra}} = \frac{1}{2} \sum_{i=1}^N \sum_{n=1}^3 \sum_{a=1}^{M_n} \mathbf{S}_i^T \mathbf{J}_n^{(a)} \mathbf{S}_{j(i, \mathbf{J}_n^{(a)})} \quad (1)$$

and

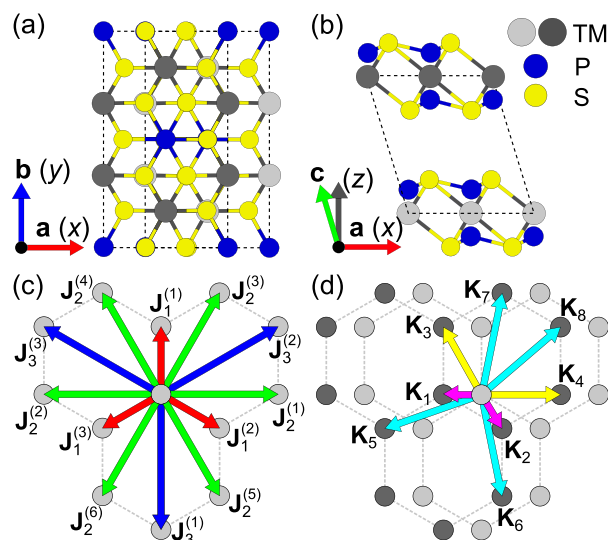


**Figure 1.** (a) Top view and (b) side view of the crystal structure of bulk TMPS<sub>3</sub>'s. The global Cartesian axes ( $x$ ,  $y$ , and  $z$ ) are defined such that the  $x$  and  $y$  directions coincide with the crystallographic directions  $a$  and  $b$ , respectively. (c) Intralayer and (d) interlayer exchange interactions considered.

$$H_{\text{exch}}^{\text{inter}} = \frac{1}{2} \sum_{i=1}^N \sum_{n=1}^8 \mathbf{S}_i^T \mathbf{K}_n \mathbf{S}_{j(i, \mathbf{K}_n)} \quad (2)$$

respectively, where the site index  $i$  runs over  $N$  magnetic atoms in the system,  $\mathbf{S}_i$  is the spin at the  $i$ th site,  $\mathbf{J}_n^{(a)}$  and  $\mathbf{K}_n$  are symmetric matrices representing anisotropic intralayer and interlayer exchange interactions, respectively, and  $\mathbf{S}_{j(i, \mathbf{J}_n^{(a)})}$  and  $\mathbf{S}_{j(i, \mathbf{K}_n)}$  denote the spins linked with  $\mathbf{S}_i$  by  $\mathbf{J}_n^{(a)}$  and  $\mathbf{K}_n$ , respectively (Figure 1c,d).  $\mathbf{J}_n^{(a)}$ 's corresponding to the nearest neighbors ( $\mathbf{J}_1^{(1-3)}$ ), second-nearest neighbors ( $\mathbf{J}_2^{(1-6)}$ ), and third-nearest neighbors ( $\mathbf{J}_3^{(1-3)}$ ) were included. In the case of  $\mathbf{K}_n$ 's, eight different interlayer exchange paths ( $\mathbf{K}_{1-8}$ ) were considered.

The next is the single-ion anisotropy ( $H_{\text{SIA}}$ ):

$$H_{\text{SIA}} = \sum_{i=1}^N \mathbf{S}_i^T \mathbf{D} \mathbf{S}_i \quad (3)$$

where  $\mathbf{D}$  is a symmetric matrix. In previous studies, a simpler version (diagonal  $\mathbf{D}$  with  $D_{xx} = D_{yy} \neq D_{zz}$ ) has been used.<sup>16,22</sup>

In FePS<sub>3</sub>, a coupling between orbital and spin polarizations ( $LS$  coupling) leads to a strong magnetic anisotropy whose magnitude is about a few tens of meV,<sup>16</sup> estimated from experimental results using crystal field theory. We therefore considered the following on-site contribution:

$$H_{LS} = \lambda \sum_{i=1}^N L_{iz} S_{iz} \quad (4)$$

where  $\lambda$  represents the  $LS$  coupling strength, and  $L_{iz}$ , which can be either 1 or  $-1$ , is the magnetic quantum number for the orbital polarization of an Fe ion.

All the parameters of  $H_{\text{exch}}^{\text{intra}}$ ,  $H_{\text{exch}}^{\text{inter}}$ ,  $H_{\text{SIA}}$ , and  $H_{LS}$  (eqs 1–4) were obtained based on DFT+ $U$  calculations; see Supporting Information for calculation details of the anisotropic magnetic models.

Because the usual DFT(+ $U$ ) methods cannot properly account for the dipolar coupling between local magnetic

moments,<sup>23</sup> we included the dipolar anisotropy ( $H_{\text{dip}}$ ) as the last constituent of our magnetic model:

$$H_{\text{dip}} = \frac{1}{2} \sum_{i=1}^N \sum_{j=1, j \neq i}^N \left[ \frac{\mathbf{m}_i \cdot \mathbf{m}_j}{r_{ij}^3} - \frac{3(\mathbf{m}_i \cdot \mathbf{r}_{ij})(\mathbf{m}_j \cdot \mathbf{r}_{ij})}{r_{ij}^5} \right] \quad (5)$$

where  $\mathbf{m}_i$  and  $\mathbf{m}_j$  are the local magnetic moments at the  $i$ th and  $j$ th sites, and  $r_{ij}$  is the distance between  $\mathbf{m}_i$  and  $\mathbf{m}_j$ ; see Supporting Information for computational details of  $H_{\text{dip}}$ .

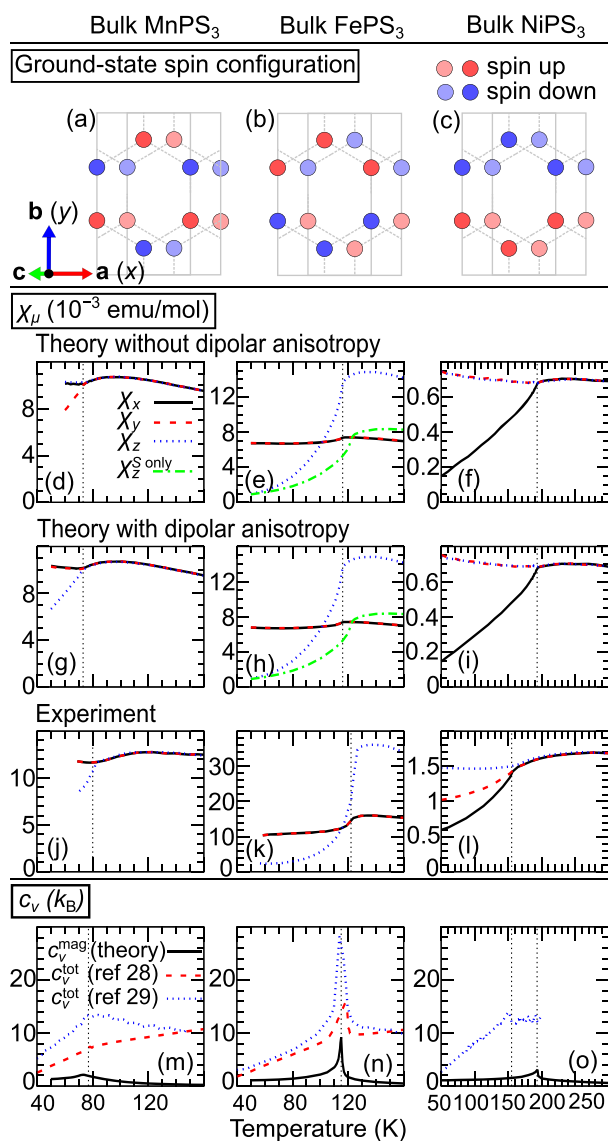
Remarkably, the ground-state ordering patterns and the directions of spin moments of all three compounds obtained from our first-principles calculations (Figure 2a–c) agree perfectly with those obtained from neutron scattering experiments.<sup>24–27</sup>

Table 1 summarizes the contributions of  $H_{\text{exch}}^{\text{intra}}$ ,  $H_{\text{exch}}^{\text{inter}}$ ,  $H_{\text{SLA}}$ ,  $H_{\text{LS}}$ , and  $H_{\text{dip}}$  to the magnetic anisotropy of bulk TMPS<sub>3</sub>. (i) In the case of MnPS<sub>3</sub>,  $H_{\text{dip}}$  and  $H_{\text{SLA}}$  dominantly contribute to the magnetic anisotropy. These two contributions are of opposite (easy-axis and easy-plane, respectively) types, and their sum results in a small easy-axis anisotropy (12.7  $\mu\text{eV}$ ) along  $z$ . Similar conclusions were drawn from previous experiments.<sup>30,31</sup> (ii) In the case of FePS<sub>3</sub>,  $H_{\text{LS}}$  dominantly gives rise to a strong easy-axis anisotropy (20.6 meV) along  $z$ . The calculated LS coupling strength  $\lambda$  (10.2 meV) matches well with the  $\lambda$  obtained from measured paramagnetic susceptibility (11.1–11.5 meV).<sup>16</sup> (iii) In the case of NiPS<sub>3</sub>, the contributions of  $H_{\text{SLA}}$ ,  $H_{\text{exch}}^{\text{intra}}$ , and  $H_{\text{dip}}$  are similar in magnitude. Their sum results in an easy-axis anisotropy (112.5  $\mu\text{eV}$ ) along  $x$ . While some studies claimed that NiPS<sub>3</sub> is best described by an XXZ model with easy-plane anisotropy,<sup>7,16</sup> our calculation results support the neutron scattering studies reporting an easy-axis anisotropy of a few hundred  $\mu\text{eV}$ <sup>22</sup> and the ordering direction of almost along  $x$ .<sup>26</sup>

Table 2 summarizes the isotropic intralayer exchange interaction  $J_n^{(a)}$  ( $= 1/3 \text{Tr } \mathbf{J}_n^{(a)}$ ) obtained from our calculations (here, the subscript  $n$  in  $J_n^{(a)}$  denotes the  $n$ th nearest neighbor). For each  $n$ , there are two groups of  $J_n^{(a)}$ , e.g.,  $J_1^{(1)}$  and  $J_2^{(2,3)}$ , which are distinguished by the  $C2/m$  symmetry of the crystal. These two groups should have different values for the isotropic exchange interactions in principle. However, since the distortion from a perfect honeycomb lattice is small, the difference between the two different values of  $J_n^{(a)}$  turns out to be small for all  $n$ 's.

In the case of MnPS<sub>3</sub> and FePS<sub>3</sub>, the calculated  $J_n^{(a)}$ 's are in good agreement with neutron scattering experiments.<sup>22</sup> In the case of NiPS<sub>3</sub>,  $J_3^{(1-3)}$ 's obtained from our calculations are larger than the value fitted with a model to experimental results,  $J_3 = 13.8 \text{ meV}$ .<sup>22</sup> (Here, we doubled this value in order to compensate the difference in the definition of  $J_3$  in ref 22 and in this study.) A rough estimate of the spin-wave gap in NiPS<sub>3</sub> is  $\sim 2S\sqrt{3\Delta J_3}$ ,<sup>22</sup> where  $\Delta$  is the single parameter that represents the total magnetic anisotropy energy per transition metal ion. Putting  $J_3 = 28 \text{ meV}$  (Table 2) and  $\Delta = 0.11 \text{ meV}$  (the magnitude of the easy-axis anisotropy in NiPS<sub>3</sub>; see Table 1) into the expression for the spin-wave gap yields 6.1 meV, which is very close to the measured spin-wave gap (7 meV).<sup>22</sup>  $J_3$  used in the experimental study is an intermediate parameter, which is indirectly estimated by a fitting procedure. On the other hand, the spin-wave gap is a directly measured quantity from neutron scattering spectra, and our calculations explain this measured gap quite well.

The classical Monte Carlo method, describing the magnetic ordering of ferromagnetic 2D materials well,<sup>32,33</sup> was employed in our study on the temperature and thickness dependence of



**Figure 2.** (a–c) Calculated ground-state spin-ordering pattern of bulk TMPS<sub>3</sub>'s. (d–l) Magnetic susceptibility of bulk TMPS<sub>3</sub>'s. The upper (d–f) and middle (g–i) panels show our calculation results, respectively, without and with considering the dipolar anisotropy. The lower (j–l) panels show the measured magnetic susceptibilities for bulk MnPS<sub>3</sub> and FePS<sub>3</sub><sup>16</sup> and for bulk NiPS<sub>3</sub>.<sup>26</sup> In the case of FePS<sub>3</sub> (e, h),  $\chi_z$  includes the effects of orbital polarizations (see also Supporting Information for computational details). (m–o) Calculated (magnetic) specific heat  $c_v^{\text{mag}}$  of bulk TMPS<sub>3</sub>'s and the experimental data for the (total) specific heat  $c_v^{\text{tot}}$ .<sup>28,29</sup> The vertical dashed lines show the estimated critical temperatures.

the thermodynamic quantities of TMPS<sub>3</sub>'s; see Supporting Information for discussions on the effects of quantum fluctuations regarding the validity of using the classical spin models in Monte Carlo simulation. Figure 2d–l shows the magnetic susceptibility of bulk TMPS<sub>3</sub>'s. The calculated  $T_N$ 's of MnPS<sub>3</sub> and FePS<sub>3</sub> are 72 and 116 K, respectively, in good agreement with experiments (80 and 120 K, respectively).<sup>16,21</sup> In the case of MnPS<sub>3</sub> (Figure 2g), not only the  $T_N$  but also the anisotropy of the magnetic susceptibility (the differences between  $\chi_x$ ,  $\chi_y$ , and  $\chi_z$ ) agrees with the experimental data (Figure 2j). As can be seen in Figure 2d,g,  $H_{\text{dip}}$  plays a crucial role in reproducing the anisotropy of the magnetic susceptibility

Table 1. Magnetic Anisotropy of Bulk TMPS<sub>3</sub>'s<sup>a</sup>

	<b>n</b>	$H_{LS}$	$H_{SIA}$	$H_{exch}^{intra}$	$H_{exch}^{inter}$	$H_{dip}$	$H_{tot}$	
MnPS <sub>3</sub>	<i>x</i>	0	−13.5	−1.4	0.1	18.6	3.8	
	<i>y</i>	0	−14.3	−1.4	−0.1	17.6	1.6	
	<i>z</i>	0.2	27.7	3.0	0.0	−36.2	−5.3	( <i>z</i> )
FePS <sub>3</sub>	<i>x</i>	0	−10	404	15.6	−44.4	365	
	<i>y</i>	0	−124	−120	−1.0	33.8	−211	
	<i>z</i>	−20416	134	−284	−14.5	10.6	−20567	( <i>z</i> )
NiPS <sub>3</sub>	<i>x</i>	0	−38.7	−21.1	−2.9	−11.9	−74.6	( <i>x</i> )
	<i>y</i>	0	−21.0	45.7	−0.2	12.4	36.9	
	<i>z</i>	−15	59.8	−24.6	3.2	0.6	39.0	

<sup>a</sup>The total energy ( $H_{tot}$ , the sum of eqs 1–5) per transition metal ion at a given ordering direction **n** (*x*, *y*, and *z* in Figure 1a,b) is shown in units of  $\mu$ eV. The parentheses in the last column show the easy-axis. The contributions of intralayer ( $H_{exch}^{intra}$ ) and interlayer ( $H_{exch}^{inter}$ ) exchange interactions, single-ion anisotropy ( $H_{SIA}$ ), LS coupling ( $H_{LS}$ ), and dipolar anisotropy ( $H_{dip}$ ) (eqs 1–5) are also shown.

Table 2. Isotropic Intralayer Exchange Interaction  $J_n^{(a)} = \frac{1}{3} \text{Tr} J_n^{(a)}$  in Units of meV<sup>a</sup>

	$J_1^{(1)}$	$J_1^{(2,3)}$	$J_2^{(1,2)}$	$J_2^{(3-6)}$	$J_3^{(1)}$	$J_3^{(2,3)}$
MnPS <sub>3</sub>	1.06	1.18	0.07	0.07	0.72	0.69
FePS <sub>3</sub>	−1.36	−1.36	0.11	0.12	2.37	2.40
NiPS <sub>3</sub>	−5.21	−5.34	−0.23	−0.20	27.4	28.2

<sup>a</sup>See Figure 1c also.

below  $T_N$ . Quite remarkably, in the case of FePS<sub>3</sub> (Figure 2h), the calculated magnetic susceptibilities reproduce the significant difference between  $\chi_z$  and  $\chi_{x,y}$  over all temperatures, in agreement with the experiment (Figure 2k). Here, we emphasize the importance of including the orbital degrees of freedom ( $L_{iz}$  in eq 4) in calculating the magnetic susceptibility: the significant enhancement of  $\chi_z$  shown in Figure 2e,h (see also Supporting Information for how the orbital contribution was considered in our Monte Carlo simulations).

In the case of NiPS<sub>3</sub> (Figure 2i), although the calculated  $T_N$  (193 K) is 38 K higher than the experimental value (155 K),<sup>16,26</sup> it is in much better agreement with experiments than previous theoretical estimations (353 and 560 K from refs 22 and 34, respectively). More importantly, our calculations reproduce several key features observed in experiments: (i) the susceptibility is very isotropic ( $\chi_x = \chi_y = \chi_z$ ) if  $T > T_N$ , (ii) there is a broad peak far above  $T_N$  at  $T \sim 250$  K, and (iii)  $\chi_x$  is the smallest if  $T < T_N$ , indicating that the antiferromagnetic order is almost along *x*.<sup>22,26</sup>

Figure 2m–o shows the magnetic specific heat ( $c_v^{\text{mag}}$ ) of bulk TMPS<sub>3</sub>. The peak in the  $c_v^{\text{mag}}$  of FePS<sub>3</sub> is much sharper than those in the other cases, in good agreement with experiments,<sup>28,29</sup> which is easily understood in that the magnetic anisotropy of FePS<sub>3</sub> is orders of magnitude larger than that of the other TMPS<sub>3</sub>'s (Table 1). We note that the measured total specific heat ( $c_v^{\text{tot}}$ ) for bulk TMPS<sub>3</sub> shown in Figure 2m–o includes the contributions arising from phonons and other possible noises and that the discrepancies between the different experimental results call for further experimental studies guided by our paper.

Now we discuss how the  $T_N$  and magnetic susceptibility change with the number of layers in few-layer FePS<sub>3</sub> and NiPS<sub>3</sub>. In Figure 3, we first notice that the magnetic phase transition exists in the monolayer (1 L) limit. The thickness dependence of the  $T_N$  significantly varies with the transition metal element. In the case of FePS<sub>3</sub>, the  $T_N$  is (almost) independent of the number

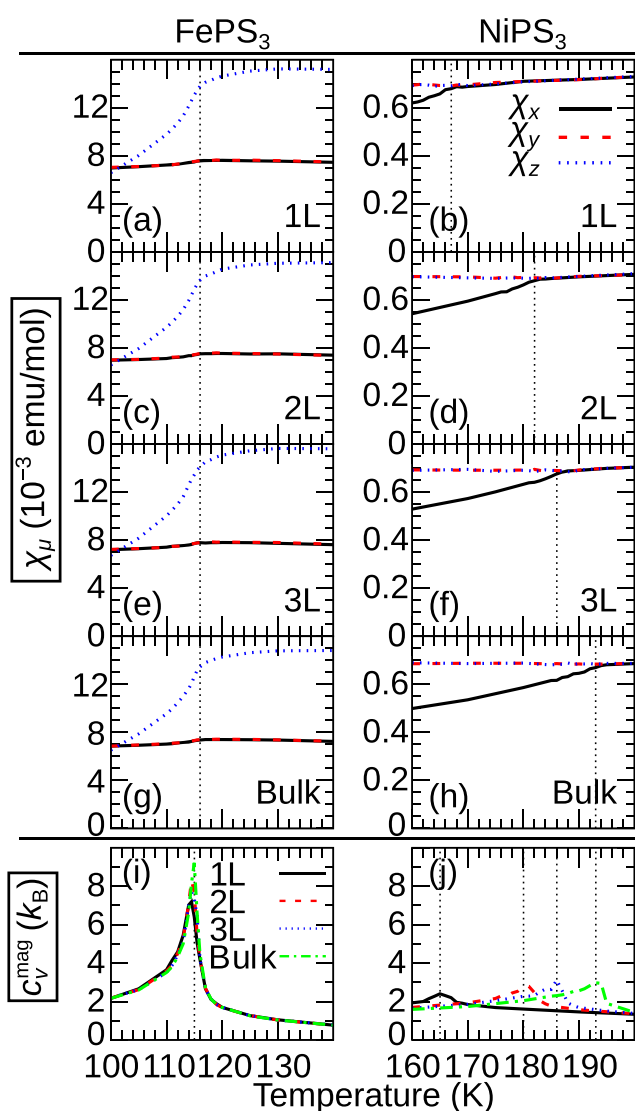


**Figure 3.** (a–h) Magnetic susceptibility of bulk and few-layer TMPS<sub>3</sub>'s. (i, j) Specific heat arising from magnetic moments  $c_v^{\text{mag}}$  of bulk and few-layer TMPS<sub>3</sub>'s. The vertical dashed lines show the estimated Néel temperatures.

of layers, also in good agreement with experiments.<sup>6</sup> The interlayer exchange interactions in FePS<sub>3</sub> (see Supporting



Information Table S4) are orders of magnitude smaller than the intralayer ones (see Table 2) and the  $LS$  coupling (see Table 1); this explains why the  $T_N$  hardly changes with the thickness.

By contrast,  $T_N^{\text{bulk}} - T_N^{\text{1L}}$  of  $\text{NiPS}_3$  (28 K) is much larger than that of  $\text{FePS}_3$  (0 K); this is easily explained by the unusually large interlayer exchange interactions of  $\text{NiPS}_3$ , especially the second-nearest-neighbor ones ( $K_{3,4} = \frac{1}{3} \text{Tr } \mathbf{K}_{3,4} \sim 1.64$  meV; see Supporting Information Table S4), which are as large as 30% of the nearest-neighbor intralayer exchange interactions ( $J_1^{(1-3)} \sim -5.3$  meV; see Table 2).

Notably, we predict a finite (and also considerably large)  $T_N$  for monolayer  $\text{NiPS}_3$  (Figure 3b,j), which indicates that the magnetic order persists in the genuine 2D limit of  $\text{NiPS}_3$ . On the other hand, a recent Raman study drew exactly the opposite conclusion that the magnetic order is absent in monolayer  $\text{NiPS}_3$  (but is present in bilayer or thicker samples),<sup>7</sup> which was largely based on their observation that the frequencies of certain Raman peaks (denoted as  $P_2$  in ref 7, the  $E_g$  modes at  $\sim 180$   $\text{cm}^{-1}$ ) did not budge with decreasing the temperature (far below the bulk  $T_N$ ) in monolayer samples while noticeably shifted in thicker samples.

At the same time, ref 7 also reported the emergence of a strong two-magnon continuum in the Raman spectrum of monolayer  $\text{NiPS}_3$ , which is a clear evidence of magnetic ordering, at similar temperatures as in thicker samples. Thus, the two seemingly contradictory experimental results have remained a puzzle so far.

Remarkably, we found that such a complete absence of the frequency shifts of  $P_2$  peaks in the Raman spectrum of magnetically ordered monolayer  $\text{NiPS}_3$  can be fully understood if the effects of the 3-fold-degenerate ground-state manifold of monolayer  $\text{NiPS}_3$ , as in other honeycomb-lattice compounds,<sup>35</sup> are considered. Our resolution of this important puzzle, together with the results of our calculations, fully explains the seemingly contradictory experimental results in ref 7 but, at the same time, disproves the conclusion therein.

In the previous Raman study,<sup>7</sup> a pair of degenerate Raman peaks (labeled as  $P_2$  in ref 7), one of which was only visible in the parallel-polarization setup  $[-z(xx)z]$  and the other only in the cross-polarization setup  $[-z(xy)z]$ , was considered an order parameter of bulk  $\text{NiPS}_3$  because a frequency difference between the two Raman peaks (denoted as  $\Delta P_2$  from now on) started to develop just below  $T_N$  and increased further as the temperature decreased while  $\Delta P_2$  was negligible above  $T_N$ . The same phenomenon was observed from the bulk down to the bilayer. In monolayers on the other hand,  $\Delta P_2$  remained zero at all temperatures. The result was then interpreted that the magnetic order is absent only in monolayer  $\text{NiPS}_3$ .

However, we realized that  $\Delta P_2$  cannot be measured from Raman experiments with the two (parallel- and cross-) polarization setups even if the magnetic order persists in monolayer  $\text{NiPS}_3$ . A monolayer  $\text{NiPS}_3$  has a 3-fold rotation symmetry (the  $D_{3d}$  point group) due to the lack of monoclinic stacking; consequently, its zigzag antiferromagnetic ground states are triply degenerate (imagine three different zigzag directions that can fit in a honeycomb lattice). An important note here is that all three degenerate states appear in a sample as magnetic domains with three different optical responses (this phenomenon is common in compounds with 3-fold ground states interconnected by 3-fold rotations<sup>35</sup>). The Raman responses of such domains should be averaged when we discuss the polarization-setup dependence of Raman peaks in monolayer  $\text{NiPS}_3$ .

The two  $P_2$  peaks are assigned to the  $E_g$  phonon mode in the  $D_{3d}$  point group and their Raman tensors, which we will denote as  $E_g^{(1)}$  and  $E_g^{(2)}$ , are respectively given by

$$\begin{pmatrix} c & 0 & 0 \\ 0 & -c & d \\ 0 & d & 0 \end{pmatrix} \quad \text{and} \quad \begin{pmatrix} 0 & -c & -d \\ -c & 0 & 0 \\ -d & 0 & 0 \end{pmatrix} \quad (6)$$

where  $c$  and  $d$  are real numbers. The Raman intensities in the parallel- and cross-polarization setups are proportional to the squares of the  $xx$  and  $xy$  components of the Raman tensors, respectively. The  $E_g^{(1)}$  mode is therefore visible only in the parallel-polarization setup, while the  $E_g^{(2)}$  mode only in the cross-polarization setup. If magnetic ordering happens, a frequency difference between the two modes develops. Since the Raman peaks can be selectively captured (by adjusting the polarizations of incoming and outgoing lights),  $\Delta P_2$  can be measured accurately no matter how broad each of the two  $P_2$  peaks is (see Figure 4a).

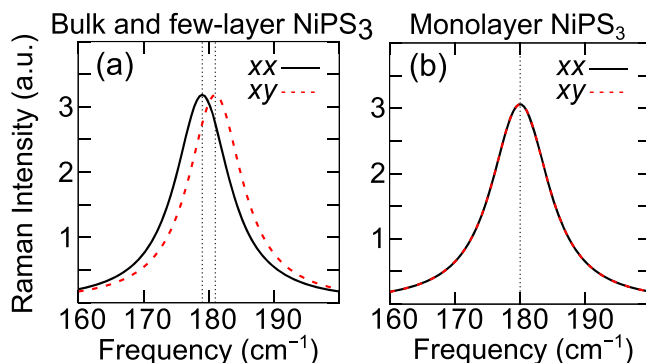


**Figure 4.** Simulated Raman spectra of  $\text{NiPS}_3$  near the  $P_2$  peaks for (a) few-layer and bulk  $\text{NiPS}_3$  (the  $C_{2h}$  point group) and (b) monolayer  $\text{NiPS}_3$  (the  $D_{3d}$  point group). It was assumed that the two peaks comprising  $P_2$  are given by Lorentzians with the same height and width, and their centers are separated by 2  $\text{cm}^{-1}$ . The half-width at half-maximum is 5  $\text{cm}^{-1}$ . These parameters were chosen to mimic the experimental results.<sup>7</sup> In the legends,  $xx$  and  $xy$  represent the parallel- and cross-polarization setups, respectively.

Note, however, that those Raman tensors are for one of the three zigzag orientations where the same-spin zigzag chains are aligned along the  $x$  direction. The Raman tensors for the other zigzag orientations can be obtained by applying  $120^\circ$  and  $240^\circ$  rotations with respect to  $z$  to the above expressions. In the case of the  $E_g^{(1)}$  mode, the Raman tensors for all the different orientations are written as

$$\begin{pmatrix} c & 0 & 0 \\ 0 & -c & d \\ 0 & d & 0 \end{pmatrix}, \begin{pmatrix} -\frac{c}{2} & -\frac{\sqrt{3}c}{2} & -\frac{\sqrt{3}d}{2} \\ -\frac{\sqrt{3}c}{2} & \frac{c}{2} & -\frac{d}{2} \\ -\frac{\sqrt{3}d}{2} & -\frac{d}{2} & 0 \end{pmatrix}, \text{ and } \begin{pmatrix} -\frac{c}{2} & \frac{\sqrt{3}c}{2} & \frac{\sqrt{3}d}{2} \\ \frac{\sqrt{3}c}{2} & \frac{c}{2} & -\frac{d}{2} \\ \frac{\sqrt{3}d}{2} & -\frac{d}{2} & 0 \end{pmatrix} \quad (7)$$

Similarly, the three  $E_g^{(2)}$  Raman tensors for the three different zigzag orientations read

$$\begin{pmatrix} 0 & -c & -d \\ -c & 0 & 0 \\ -d & 0 & 0 \end{pmatrix}, \begin{pmatrix} \frac{\sqrt{3}c}{2} & \frac{c}{2} & \frac{d}{2} \\ \frac{c}{2} & -\frac{\sqrt{3}c}{2} & \frac{\sqrt{3}d}{2} \\ \frac{d}{2} & \frac{\sqrt{3}d}{2} & 0 \end{pmatrix}, \text{ and } \begin{pmatrix} -\frac{\sqrt{3}c}{2} & \frac{c}{2} & \frac{d}{2} \\ \frac{c}{2} & \frac{\sqrt{3}c}{2} & -\frac{\sqrt{3}d}{2} \\ \frac{d}{2} & -\frac{\sqrt{3}d}{2} & 0 \end{pmatrix} \quad (8)$$

Element-wise square-averaging of the Raman tensors over the three zigzag orientations now yields the following intensity matrices

$$\begin{pmatrix} \frac{c^2}{2} & \frac{c^2}{2} & \frac{d^2}{2} \\ \frac{c^2}{2} & \frac{c^2}{2} & \frac{d^2}{2} \\ \frac{d^2}{2} & \frac{d^2}{2} & 0 \end{pmatrix} \text{ and } \begin{pmatrix} \frac{c^2}{2} & \frac{c^2}{2} & \frac{d^2}{2} \\ \frac{c^2}{2} & \frac{c^2}{2} & \frac{d^2}{2} \\ \frac{d^2}{2} & \frac{d^2}{2} & 0 \end{pmatrix} \quad (9)$$

respectively, for  $E_g^{(1)}$  and  $E_g^{(2)}$ . Here, the  $xx$  ( $xy$ ) components of these two matrices give the domain-averaged Raman intensities for  $E_g^{(1)}$  and  $E_g^{(2)}$ , respectively, in the parallel- (cross-) polarization setup. Remarkably, (i) these two matrices are exactly the same and (ii) their  $xx$  and  $xy$  components are also the same. An important point here is that there is certainly no polarization selection rule for the  $E_g^{(1)}$  and  $E_g^{(2)}$  modes if the averaging effects of the magnetic domains are taken into account: the two peaks comprising the  $P_2$  peak are to be observed with equal intensities regardless of whether the parallel- or cross-polarization setup is used.

Such a disappearance of the polarization-setup dependence has a huge impact on detecting  $\Delta P_2$  in practice; the impact is much more dramatic when the broadness of the two peaks

comprising the  $P_2$  peak is similar to or even larger than their frequency difference ( $\Delta P_2$ ). If that condition is met, the two peaks appear to be just one peak. Unfortunately, the splitting in the peaks  $\Delta P_2$  measured in ref 7 were at most  $\sim 2 \text{ cm}^{-1}$  (in few-layer and bulk  $\text{NiPS}_3$ ), and the half-width at half-maximum of the  $P_2$  peaks in monolayer  $\text{NiPS}_3$  was at least  $5 \text{ cm}^{-1}$ . Given that condition,  $\Delta P_2$  cannot be measured because of the large overlap between the peaks as shown in Figure 4b.

In summary, our anisotropic magnetic model with an unprecedentedly large number of parameters determined from extensive first-principles calculations and classical Monte Carlo simulations with special handling of the orbital polarization effects explained the magnetic structure, critical temperature, susceptibility, and specific heat of bulk and few-layer  $\text{TMPS}_3$ 's reported from experiments. Moreover, we have shown that the criterion used to judge magnetic ordering in the recent Raman study of  $\text{NiPS}_3$ <sup>7</sup> is invalid in the case of monolayer samples and that magnetic ordering in  $\text{NiPS}_3$  persists down to the monolayer limit. Recently, direct measurements of the magnetic susceptibility of 2D materials were carried out.<sup>36</sup> Thus, our predictions on the thickness dependence of the thermodynamic quantities of few-layer  $\text{TMPS}_3$ 's can be verified immediately, which will allow a deeper understanding of magnetic ordering in atomically thin 2D materials, a fundamental issue of the Mermin–Wagner theorem.<sup>13</sup>

## ■ ASSOCIATED CONTENT

### Supporting Information

The Supporting Information is available free of charge at <https://pubs.acs.org/doi/10.1021/acs.nanolett.1c03992>.

Calculation details of anisotropic magnetic model, dipolar anisotropy, and Monte Carlo simulations; additional comments on calculated exchange interactions; discussion of the effects of LS coupling on the magnetic anisotropy and the related numerical issues; a detailed derivation of the formulas that evaluate the magnetic susceptibility and specific heat of  $\text{FePS}_3$  with a consideration of the orbital degrees of freedom; and the quantum fluctuation effects in monolayer  $\text{NiPS}_3$  (PDF)

## ■ AUTHOR INFORMATION

### Corresponding Authors

**Tae Yun Kim** – Center for Correlated Electron Systems, Institute for Basic Science, Seoul 08826, Korea; Department of Physics and Astronomy, Seoul National University, Seoul 08826, Korea; Center for Theoretical Physics, Seoul National University, Seoul 08826, Korea; [orcid.org/0000-0001-8371-0654](https://orcid.org/0000-0001-8371-0654); Email: [kimtaeyun@outlook.com](mailto:kimtaeyun@outlook.com)

**Cheol-Hwan Park** – Center for Correlated Electron Systems, Institute for Basic Science, Seoul 08826, Korea; Department of Physics and Astronomy, Seoul National University, Seoul 08826, Korea; Center for Theoretical Physics, Seoul National University, Seoul 08826, Korea; [orcid.org/0000-0003-1584-6896](https://orcid.org/0000-0003-1584-6896); Email: [cheolhwan@snu.ac.kr](mailto:cheolhwan@snu.ac.kr)

Complete contact information is available at:

<https://pubs.acs.org/doi/10.1021/acs.nanolett.1c03992>

### Notes

The authors declare no competing financial interest.

## ■ ACKNOWLEDGMENTS

We thank Je-Geun Park and Hyeonsik Cheong for many fruitful discussions during our previous collaborations and Choong H. Kim for helpful discussions. This work was supported by the Creative-Pioneering Research Program through Seoul National University, Korean NRF No-2020R1A2C1014760, and the Institute for Basic Science (Grant IBSR009-D1). Computational resources were provided by KISTI Supercomputing Center (Grant KSC-2020-INO-0078).

## ■ REFERENCES

- (1) Gong, C.; Li, L.; Li, Z.; Ji, H.; Stern, A.; Xia, Y.; Cao, T.; Bao, W.; Wang, C.; Wang, Y.; Qiu, Z. Q.; Cava, R. J.; Louie, S. G.; Xia, J.; Zhang, X. Discovery of Intrinsic Ferromagnetism in Two-Dimensional van Der Waals Crystals. *Nature* **2017**, *546*, 265–269.
- (2) Huang, B.; Clark, G.; Navarro-Moratalla, E.; Klein, D. R.; Cheng, R.; Seyler, K. L.; Zhong, D.; Schmidgall, E.; McGuire, M. A.; Cobden, D. H.; Yao, W.; Xiao, D.; Jarillo-Herrero, P.; Xu, X. Layer-Dependent Ferromagnetism in a van Der Waals Crystal down to the Monolayer Limit. *Nature* **2017**, *546*, 270–273.
- (3) Lee, S.; Choi, K.-Y.; Lee, S.; Park, B. H.; Park, J.-G. Tunneling Transport of Mono- and Few-Layers Magnetic van Der Waals MnPS<sub>3</sub>. *APL Mater.* **2016**, *4*, 086108.
- (4) Du, K.-z.; Wang, X.-z.; Liu, Y.; Hu, P.; Utama, M. I. B.; Gan, C. K.; Xiong, Q.; Kloc, C. Weak van Der Waals Stacking, Wide-Range Band Gap, and Raman Study on Ultrathin Layers of Metal Phosphorus Trichalcogenides. *ACS Nano* **2016**, *10*, 1738–1743.
- (5) Kuo, C.-T.; Neumann, M.; Balamurugan, K.; Park, H. J.; Kang, S.; Shiu, H. W.; Kang, J. H.; Hong, B. H.; Han, M.; Noh, T. W.; Park, J.-G. Exfoliation and Raman Spectroscopic Fingerprint of Few-Layer NiPS<sub>3</sub> Van Der Waals Crystals. *Sci. Rep.* **2016**, *6*, 20904.
- (6) Lee, J.-U.; Lee, S.; Ryoo, J. H.; Kang, S.; Kim, T. Y.; Kim, P.; Park, C.-H.; Park, J.-G.; Cheong, H. Ising-Type Magnetic Ordering in Atomically Thin FePS<sub>3</sub>. *Nano Lett.* **2016**, *16*, 7433–7438.
- (7) Kim, K.; Lim, S. Y.; Lee, J.-U.; Lee, S.; Kim, T. Y.; Park, K.; Jeon, G. S.; Park, C.-H.; Park, J.-G.; Cheong, H. Suppression of Magnetic Ordering in XXZ-Type Antiferromagnetic Monolayer NiPS<sub>3</sub>. *Nat. Commun.* **2019**, *10*, 345.
- (8) Kim, K.; Lim, S. Y.; Kim, J.; Lee, J.-U.; Lee, S.; Kim, P.; Park, K.; Son, S.; Park, C.-H.; Park, J.-G.; Cheong, H. Antiferromagnetic Ordering in van Der Waals 2D Magnetic Material MnPS<sub>3</sub> Probed by Raman Spectroscopy. *2D Mater.* **2019**, *6*, 041001.
- (9) Lim, S. Y.; Kim, K.; Lee, S.; Park, J.-G.; Cheong, H. Thickness Dependence of Antiferromagnetic Phase Transition in Heisenberg-Type MnPS<sub>3</sub>. *Curr. Appl. Phys.* **2021**, *21*, 1–5.
- (10) Kang, S.; et al. Coherent Many-Body Exciton in van Der Waals Antiferromagnet NiPS<sub>3</sub>. *Nature* **2020**, *583*, 785–789.
- (11) Hwangbo, K.; Zhang, Q.; Jiang, Q.; Wang, Y.; Fonseca, J.; Wang, C.; Diederich, G. M.; Gamelin, D. R.; Xiao, D.; Chu, J.-H.; Yao, W.; Xu, X. Highly Anisotropic Excitons and Multiple Phonon Bound States in a van Der Waals Antiferromagnetic Insulator. *Nat. Nanotechnol.* **2021**, *16*, 655–660.
- (12) Zhang, Q.; Hwangbo, K.; Wang, C.; Jiang, Q.; Chu, J.-H.; Wen, H.; Xiao, D.; Xu, X. Observation of Giant Optical Linear Dichroism in a Zigzag Antiferromagnet FePS<sub>3</sub>. *Nano Lett.* **2021**, *21*, 6938–6945.
- (13) Mermin, N. D.; Wagner, H. Absence of Ferromagnetism or Antiferromagnetism in One- or Two-Dimensional Isotropic Heisenberg Models. *Phys. Rev. Lett.* **1966**, *17*, 1133–1136.
- (14) Berezinskii, V. L. Destruction of Long-Range Order in One-Dimensional and Two-Dimensional Systems Possessing a Continuous Symmetry Group. II. Quantum Systems. *Sov. J. Exp. Theor. Phys.* **1972**, *34*, 610.
- (15) Kosterlitz, J. M.; Thouless, D. J. Ordering, Metastability and Phase Transitions in Two-Dimensional Systems. *J. Phys. C: Solid State Phys.* **1973**, *6*, 1181–1203.
- (16) Joy, P. A.; Vasudevan, S. Magnetism in the Layered Transition-Metal Thiophosphates MPS<sub>3</sub> (M = Mn, Fe, and Ni). *Phys. Rev. B: Condens. Matter Mater. Phys.* **1992**, *46*, 5425–5433.
- (17) Vaclavkova, D.; Delhomme, A.; Faugeras, C.; Potemski, M.; Bogucki, A.; Suffczyński, J.; Kossacki, P.; Wildes, A. R.; Grémaud, B.; Saúl, A. Magnetoelastic Interaction in the Two-Dimensional Magnetic Material MnPS<sub>3</sub> Studied by First Principles Calculations and Raman Experiments. *2D Mater.* **2020**, *7*, 035030.
- (18) Olsen, T. Magnetic Anisotropy and Exchange Interactions of Two-Dimensional FePS<sub>3</sub>, NiPS<sub>3</sub> and MnPS<sub>3</sub> from First Principles Calculations. *J. Phys. D: Appl. Phys.* **2021**, *54*, 314001.
- (19) Bacaksiz, C.; Šabani, D.; Menezes, R. M.; Milošević, M. V. Distinctive Magnetic Properties of CrI<sub>3</sub> and CrBr<sub>3</sub> Monolayers Caused by Spin-Orbit Coupling. *Phys. Rev. B: Condens. Matter Mater. Phys.* **2021**, *103*, 125418.
- (20) Nauman, M.; Kiem, D. H.; Lee, S.; Son, S.; Park, J.-G.; Kang, W.; Han, M. J.; Jo, Y. Complete Mapping of Magnetic Anisotropy for Prototype Ising van Der Waals FePS<sub>3</sub>. *2D Mater.* **2021**, *8*, 035011.
- (21) Brec, R. In *Intercalation in Layered Materials*; Dresselhaus, M. S., Ed.; Springer, 1986; pp 93–124.
- (22) Lançon, D.; Ewings, R. A.; Guidi, T.; Formisano, F.; Wildes, A. R. Magnetic Exchange Parameters and Anisotropy of the Quasi-Two-Dimensional Antiferromagnet NiPS<sub>3</sub>. *Phys. Rev. B: Condens. Matter Mater. Phys.* **2018**, *98*, 134414.
- (23) Pellegrini, C.; Müller, T.; Dewhurst, J. K.; Sharma, S.; Sanna, A.; Gross, E. K. U. Density Functional Theory of Magnetic Dipolar Interactions. *Phys. Rev. B: Condens. Matter Mater. Phys.* **2020**, *101*, 144401.
- (24) Kurosawa, K.; Saito, S.; Yamaguchi, Y. Neutron Diffraction Study on MnPS<sub>3</sub> and FePS<sub>3</sub>. *J. Phys. Soc. Jpn.* **1983**, *52*, 3919–3926.
- (25) Lançon, D.; Walker, H. C.; Ressouche, E.; Ouladdiaf, B.; Rule, K. C.; McIntyre, G. J.; Hicks, T. J.; Rønnow, H. M.; Wildes, A. R. Magnetic Structure and Magnon Dynamics of the Quasi-Two-Dimensional Antiferromagnet FePS<sub>3</sub>. *Phys. Rev. B: Condens. Matter Mater. Phys.* **2016**, *94*, 214407.
- (26) Wildes, A. R.; Simonet, V.; Ressouche, E.; McIntyre, G. J.; Avdeev, M.; Suard, E.; Kimber, S. A. J.; Lançon, D.; Pepe, G.; Moubarki, B.; Hicks, T. J. Magnetic Structure of the Quasi-Two-Dimensional Antiferromagnet NiPS<sub>3</sub>. *Phys. Rev. B: Condens. Matter Mater. Phys.* **2015**, *92*, 224408.
- (27) Lane, C.; Zhu, J.-X. Thickness Dependence of Electronic Structure and Optical Properties of a Correlated van Der Waals Antiferromagnetic NiPS<sub>3</sub> Thin Film. *Phys. Rev. B: Condens. Matter Mater. Phys.* **2020**, *102*, 075124.
- (28) Takano, Y.; Arai, N.; Arai, N.; Takahashi, Y.; Takase, K.; Sekizawa, K. Magnetic Properties and Specific Heat of MPS<sub>3</sub> (M=Mn, Fe, Zn). *J. Magn. Magn. Mater.* **2004**, *272–276*, E593–E595.
- (29) Šiškins, M.; Lee, M.; Mañas-Valero, S.; Coronado, E.; Blanter, Y. M.; van der Zant, H. S. J.; Steeneken, P. G. Magnetic and Electronic Phase Transitions Probed by Nanomechanical Resonators. *Nat. Commun.* **2020**, *11*, 2698.
- (30) Wildes, A. R.; Rønnow, H. M.; Roessli, B.; Harris, M. J.; Godfrey, K. W. Anisotropy and the Critical Behaviour of the Quasi-2D Antiferromagnet, MnPS<sub>3</sub>. *J. Magn. Magn. Mater.* **2007**, *310*, 1221–1223.
- (31) Hicks, T. J.; Keller, T.; Wildes, A. R. Magnetic Dipole Splitting of Magnon Bands in a Two Dimensional Antiferromagnet. *J. Magn. Magn. Mater.* **2019**, *474*, 512–516.
- (32) Torelli, D.; Thygesen, K. S.; Olsen, T. High Throughput Computational Screening for 2D Ferromagnetic Materials: The Critical Role of Anisotropy and Local Correlations. *2D Mater.* **2019**, *6*, 045018.
- (33) Olsen, T. Theory and Simulations of Critical Temperatures in CrI<sub>3</sub> and Other 2D Materials: Easy-Axis Magnetic Order and Easy-Plane Kosterlitz–Thouless Transitions. *MRS Commun.* **2019**, *9*, 1142–1150.
- (34) Chittari, B. L.; Park, Y.; Lee, D.; Han, M.; MacDonald, A. H.; Hwang, E.; Jung, J. Electronic and Magnetic Properties of Single-Layer MPX<sub>3</sub> Metal Phosphorous Trichalcogenides. *Phys. Rev. B: Condens. Matter Mater. Phys.* **2016**, *94*, 184428.

- (35) Sears, J. A.; Zhao, Y.; Xu, Z.; Lynn, J. W.; Kim, Y.-J. Phase Diagram of  $\alpha$ -RuCl<sub>3</sub> in an in-Plane Magnetic Field. *Phys. Rev. B: Condens. Matter Mater. Phys.* **2017**, 95, No. 180411(R).
- (36) Wong, P. K. J.; et al. Evidence of Spin Frustration in a Vanadium Diselenide Monolayer Magnet. *Adv. Mater.* **2019**, 31, 1901185.